Author

Loren Chang's first undergraduate research experience led to a dead end when he learned that plasma physics was not his passion. However, when he began work in the wavefront sensing lab under Professor Chanan, he knew he had found a match to his interests. Loren's research in the testing of telescope phasing algorithms developed during his sophomore year and eventually resulted in his current pursuit of graduate studies in atmospheric remote sensing systems at the University of Colorado, Boulder. In his free time, Loren enjoys a wide range of leisure activities including astronomy, computers, swimming, cycling, hiking, and traveling to new places.

Key Terms

- Angular Resolution
- Fraunhofer Diffraction
- Gaussian Bandpass
- Mach-Zehnder Interferometer
- Phasing Algorithm
- Piston Error
- Segmented Telescope Mirror

Phasing Segmented Telescope Mirrors with a Mach-Zehnder Interferometer

Loren Chang
Physics

Abstract

With the introduction of large telescope mirrors comprised of many individual segments, the problem of insuring a smooth continuous mirror surface (i.e. phasing) becomes critical. The vertical displacements (piston errors) between the individual segments must be reduced to a small fraction of the wavelength of incoming light. In one proposed technique, light from the telescope mirror is split between the two arms of a Mach-Zehnder interferometer, and the two outputs are subtracted from one another. The piston error of each mirror segment can then be determined from the resulting fringes that occur at the segment edges of this "differential interferogram." By implementing this algorithm via computer simulation, it can be demonstrated that the dependence of fringe intensity on the piston error is a sine function when the light is monochromatic. In addition, the original algorithm may be modified to work using wavelengths of light in a Gaussian bandpass. Unlike the monochromatic case, the intensities in the broadband case behave as a sine function modulated so they decay to zero as the piston error increases. This allows for a more robust algorithm that is much more effective at detecting piston errors greater than one wavelength.

Faculty Mentor

Loren Chang's research was concerned with aligning the next generation of giant optical telescopes, which will consist of segmented primary mirrors with hundreds or even thousands of mirror segments. We know how to solve this problem for the current generation of large telescopes, such as the two Keck telescopes on Mauna Kea. However, these have only 36 segments each, and it is not clear that the same techniques will work with much larger numbers of segments. A group at the European Southern Observatory (ESO) has developed an alternative technique. Loren confirmed that the ESO simulations were substantially correct (already an admirable achievement for an undergraduate thesis). However, he went beyond this and showed how an instability in the ESO method could be addressed by using "white light," in which multiple wavelengths are sampled in parallel, rather than in series. Loren's work (among other ideas) will be featured in a collaboration meeting between UC and ESO astronomers planned for this summer.

Gary Chanan
School of Physical Sciences

Introduction

Until two decades ago, nearly all telescopes contained monolithic telescope mirrors, which are mirrors comprised of a single slab of glass. The angular resolution of a telescope mirror at light wavelength λ is given by the familiar relation λ/D (Rayleigh's Criterion). Thus, a telescope of larger diameter will have a higher resolving power, allowing it to accurately image smaller details. The needs of the astronomical community have led to the development of telescopes with mirrors of ever-greater diameter.

Unfortunately, a monolithic telescope mirror in a ground-based telescope is limited by the amount of glass required to prevent it from sagging or breaking under its weight. As the diameter of a monolithic mirror is increased, the thickness of the mirror must also be increased. Eventually, the sheer size and weight of the glass required makes this impractical for use in ground-based telescopes above a certain diameter (Nelson et al., 1985). Similarly, this property of monolithic mirrors also renders them impractical for use in larger space-based platforms due to spacecraft weight considerations.

This limitation has been overcome with the development of segmented telescope mirrors, a concept originally proposed by Nelson *et al.* for use in the Keck Telescopes (Nelson et al., 1985; Nelson, 1989). In a segmented telescope mirror, several smaller hexagonal mirror segments are placed side-by-side forming a single, continuous main mirror. Because of their smaller individual size, the individual segments do not need to be as thick as a single monolithic mirror with the same total diameter. With the weight limitation removed, the construction of extremely large telescopes becomes possible. Besides ground-based telescopes, segmented telescope mirrors are also attractive for space-based platforms due to their low mass (when compared to a monolithic mirror), and their ability to be folded before deployment. Both of these are important considerations when launching payloads into orbit.

Segmented mirror technology has already been introduced and is in use at the 10-meter Keck Telescopes in Hawaii. It is planned for the main mirror of the James Webb Space Telescope (6.5 meters in diameter), which is scheduled for launch in 2011. Other projects currently in development such as CELT (California Extremely Large Telescope) and the European Southern Observatory's 100-meter OWL (Overwhelmingly Large Telescope) are also being designed to use segmented mirrors.

Although promising when compared to monolithic mirrors, segmented mirrors are not without their own problems. The most notable of these is ensuring a smooth continuous mirror surface, a process known as phasing. A properly phased telescope will have a resolution that corresponds to the total diameter of the entire segmented mirror. Conversely, an unphased telescope will have very poor resolution, limited by the diameter of an individual segment.

One important process in phasing a segmented mirror telescope involves the vertical displacements (piston error) between adjacent segments. If the piston errors between the segments are greater than approximately $\lambda/20$ (where λ is the wavelength of light), then D is equal to the diameter of a single mirror segment. Only when the piston errors are reduced below $\lambda/20$ is D given by the total diameter of the entire segmented mirror (Chanan, 2004). In other words, the full angular resolution of the entire segmented mirror is attained only when the piston errors between the segments are smaller than $\lambda/20$.

Clearly, it is imperative that the piston errors be reduced to less than $\lambda/20$ if the optimal resolution offered by the segmented mirror is to be achieved. While each mirror segment may be raised and lowered independently of the others by a set of actuators underneath, the issue of accurately determining the piston errors between the segments to a high enough precision is non-trivial. For infrared wavelengths under which atmospheric distortion is not an issue, the required precision is on the order of 0.1 microns. A human hair, in comparison, is approximately 30 microns in thickness. This has necessitated the development of what are known as phasing algorithms: operations used to detect and correct for discontinuities between mirror segments through the analysis of various diffraction phenomena along the segment edges.

Successful detection of piston errors has been achieved in the current algorithm used at the Keck Telescopes developed by Chanan *et al.* (henceforth referred to as the Keck algorithm). The Keck algorithm relies on the analysis of diffraction patterns generated by placing a mask that defines small circular subapertures directly above the segment edges and analyzing the resulting diffraction patterns. This algorithm has been shown to be reliable in phasing a segmented mirror to a root mean square piston error of less than 0.1 microns (Chanan, 1988). However, the Keck algorithm requires the tight centering of the mask such that the circular subapertures are at the centers of the intersegment edges. The number of masks and subapertures must also be increased as the number of mirror segments is increased,

which may prove to be problematic in larger segmented mirror telescopes such as OWL.

To resolve the aforementioned problem, another algorithm for detecting piston errors has been proposed for use in OWL by Martinez *et al.* (2002) at the European Southern Observatory and *Laboratoire d' Astrophysique de Marseille.* This algorithm involves the use of a specially tuned Mach-Zehnder interferometer and is notable for its absence of a mask above the segment edges, as in the Keck and other phasing algorithms. This lack of a mask should, in theory, simplify the setup and analysis involved in determining the intersegment piston error.

While promising, the original Mach-Zehnder algorithm (hereafter referred to as the monochromatic algorithm) does contain some pitfalls. Specifically, there is a significant ambiguity in determining the actual piston error due to aliasing, especially at large piston errors. Essentially, it becomes impossible to determine the exact piston error when the error is greater than one wavelength.

In this study, the original monochromatic algorithm was reproduced by using a computer-simulated segmented mirror whose segments could be individually displaced to simulate piston errors of various values. The original algorithm was then modified to use a Gaussian bandpass (light of several wavelengths in a Gaussian distribution about a central wavelength rather than just a single wavelength). This new broadband algorithm addresses the flaws of the monochromatic algorithm, as it does not suffer from ambiguity over piston errors greater than one wavelength. It simultaneously retains the advantages of the monochromatic algorithm since it does not require the presence of a mask, as with the Keck algorithm.

Monochromatic Mach-Zehnder Algorithm

Overview
In the monochromatic algorithm, monochromatic light from the telescope mirror is passed through a specially-tuned Mach-Zehnder interferometer (Figure 1).

In a Mach-Zehnder interferometer, light is split between two arms, with a phase shift of π introduced each time the light strikes a mirror (recall that waves incident on a denser medium are phase shifted in this manner). By summing the phase differences and recombining at the outputs, it can be shown that the above setup results in constructive interference at one interferogram and complete destructive interference at the other.
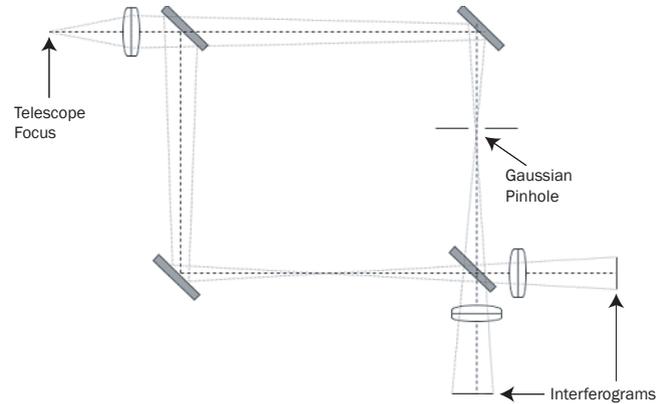

Figure 1
Mach-Zehnder Interferometer Setup

For the monochromatic phasing algorithm, an optical path difference of l/4 is introduced between the two arms of the interferometer, while a pinhole is placed in one of the arms. The pinhole has a Gaussian profile to eliminate diffraction artifacts that would otherwise result with the sharp edges of a circular pinhole. The pinhole acts as a low-pass filter, whereas the entire interferometer acts as a high-pass filter on recombination due to the phase shifts introduced as a result of reflection.

The output interferograms are then subtracted from one another, forming what is referred to as a "differential interferogram." This differential interferogram will then contain a series of fringes along the segment edges, as shown by the simulated images in Figure 2. It will be demonstrated that the piston error between adjacent segments can be extracted from the intensities of these fringes, which we refer to as the "peak to valley" (PtV) value.

Mathematical Background
The electric fields at the interferograms may be described by this equation:

$$A_1 = C_1 e^{ik(\varphi_1 + \alpha)} + C_2 e^{ik\varphi_2}$$
$$A_2 = C_1 e^{ik(\varphi_1 + \alpha)} - C_2 e^{ik\varphi_2}$$

(1)

where k is the wave number of our monochromatic light, $C1$ and $C2$ are the amplitudes of light from the two arms, $\varphi1$ and $\varphi2$ are the phases from the two arms, and α is the constant optical path difference introduced between the arms.

The interferogram intensities I_1 and I_2 may then be determined simply by squaring Equation 1:

$$I_1 = \left| A_1 A_1^* \right| = C_1^2 + C_2^2 + 2C_1 C_2 \cos[k(\varphi_1 - \varphi_2 + \alpha)]$$
$$I_2 = \left| A_2 A_2^* \right| = C_1^2 + C_2^2 - 2C_1 C_2 \cos[k(\varphi_1 - \varphi_2 + \alpha)]$$

(2)

Subtracting the two interferogram intensities gives the intensity at the differential interferogram:

$$I_1 - I_2 = 4A_1A_2 \cos[k(\varphi_1 - \varphi_2 + \alpha)] \quad (3)$$

Notice that the constant offsets are thus removed while the intensity of the cosine term is increased by a factor of two.

Finally, redefining ($\varphi_1 - \varphi_2$) as the piston error δ, and consolidating the constant coefficients as a single constant term V, the above equation may be rewritten as:

$$\nu(\delta) = V \cos[k(\delta + \alpha)] \quad (4)$$

Thus, the PtV value ν will be proportional to the cosine of the phase difference resulting from the piston error. By setting the optical path difference α equal to $\lambda/4$, the argument of the cosine function is phase shifted by $\pi/2$, converting the cosine to a sine. This allows for the determination of the relative positions of adjacent segments, which is demonstrated by the simulation.

Simulation

The interferograms resulting from the Mach-Zehnder wavefront sensor detailed above were simulated via computer. The simulation verifies the analysis and provides a unique opportunity to modify parameters in a strictly controlled environment, while allowing further insight into some of the processes that occur. In the future, it will also be easier to implement the effects of atmospheric distortion by computer rather than by analysis.

The conditions in the wavefront sensor can be approximated using Fraunhofer diffraction, which assumes that the distances involved are long enough to result in plane waves. The Fraunhofer diffraction pattern on the image plane is given by performing a Fourier transform on the incoming wavefront (Hecht, 2001). The wavefronts passing through each of the two arms of the interferometer must thus be Fourier transformed twice to generate the final amplitudes at the interferograms.

A quick look at this process provides some insight on the function of the pinhole. By per-
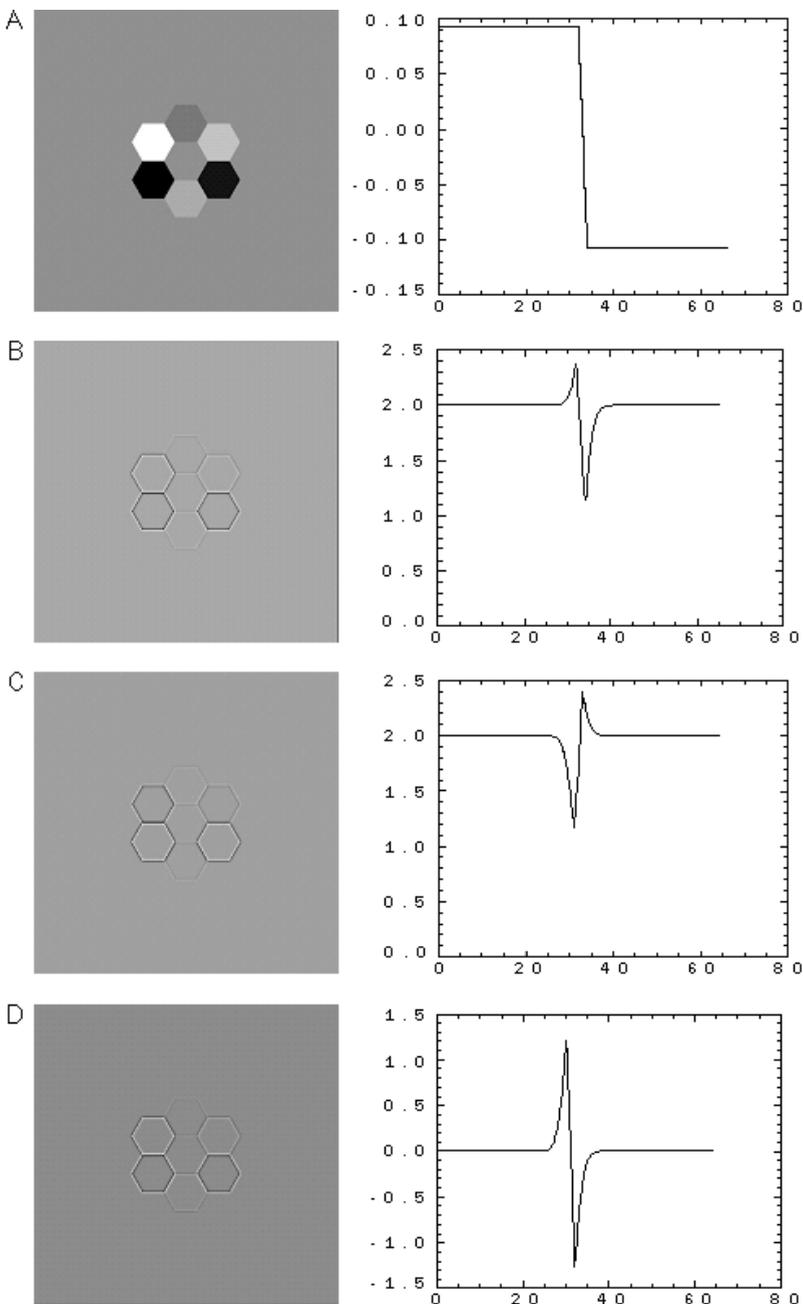

Figure 2
Simulated Images: Images in the left column show simulated 2-D images. Images in the right column are plots of cuts across segment edges.

A)   Map of Physical Step Heights

B)   Output from One Interferogram

C)   Output from the Other Interferogram

D)   Differential Interferogram, the Difference between the Two Peaks on the Right Image is the PtV Value

forming a Fourier transform on the wavefront, it is essentially decomposed into spatial frequencies. The result is the removal of high frequency contributions, effectively creating a low-pass filter. By performing an inverse Fourier transform on the filtered function and then subtracting it from the unfiltered function from the other arm, the result is essentially a high-pass filter.

The Fourier transform can be calculated numerically to a high degree of precision using the Fast Fourier Transform (FFT) algorithm.

Using the above as a basis for the simulation algorithm, a simulation for the interferogram outputs was created through the following process:

1) A two-dimensional map of a segmented mirror was generated, with each segment having a distinct piston error.
2) The map was then used to generate the values of the actual electromagnetic waves. The setup calls for two interferograms, each consisting of the superposition of one wavefront from each of the two arms. Four complex wavefronts were also needed, each containing its respective phase shifts due to reflection and the introduced optical path difference of $\lambda/4$.
3) An inverse Fourier transform was performed on the aperture functions that had just been generated to bring the wavefronts to the focal point. The amplitudes of the two wavefronts in the arm containing the pinhole were scaled to account for the spatial filtering by the pinhole.
4) Finally, the Fourier transform of the four aperture functions was taken to bring them to the output plane. The appropriate wavefronts were summed and squared to generate the intensities of the interferograms. The two resulting interferograms were then subtracted from one another to create the differential interferogram.

Notice distinctive fringes that result along the segment edges in the differential interferogram (Figure 2D). It is the distance between the amplitudes of these two peaks that we are concerned with, and it is this value that is denoted in previous derivation by ν (referred to as the PtV by Martinez et al., 2002) The sign of ν is simply a matter of convention.

Simulation Results

Differential interferograms corresponding to various values of piston error were generated and the PtV values were measured as shown in Figure 3.
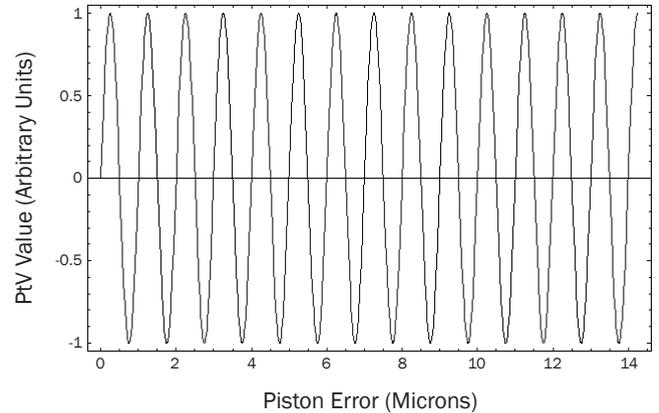

Figure 3
Results of PtV (n) from simulation (vertical axis), plotted with respect to physical step height (horizontal axis), for λ = 1 micron. As expected, the PtV values are related to the sine of the piston error.

The simulation results show strong agreement with the values predicted via the mathematical derivation detailed previously. Recall that if the optical path difference α is set to $\lambda/4$ as in our setup, then ν is given by:

$$\nu(\delta) = V \sin[k\delta] \qquad (5)$$

Analysis

The monochromatic algorithm detailed above provides a relation between the intersegment piston error and the PtV intensity. However, a closer analysis shows that some significant drawbacks remain.

The sine function is strictly periodic and repeats itself at distances in phase separated by integer multiples of λ (recall that the sign of the PtV is also taken into account). Therefore it will be impossible to differentiate between a phase step of δ and $\delta+\lambda$.

Martinez *et al.* (2002) proposed to remedy this ambiguity through the separate use of two or more discrete wavelengths of light and determining the piston error from the relative PtV values at the two different wavelengths. However, this method is again limited by the periodic nature of the sine functions, as the relative values will repeat after a certain distance (Figure 4). While it has been demonstrated that this distance can be increased above the desired capture range by careful selection of which wavelengths to use, it is still worth exploring other methods that will not be affected by this problem.
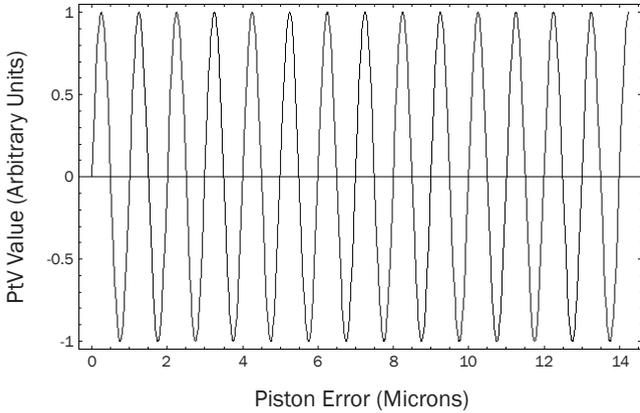
Figure 4
PtV at 1 (blue line) and 2 (red line) microns plotted with respect to phase step. Notice the repetition of relative PtV values.

Broadband Mach-Zehnder Algorithm

Overview
To eliminate the ambiguities in the monochromatic Mach-Zehnder algorithm, light in a Gaussian bandpass is used in place of monochromatic light, with the setup and analysis the same as the monochromatic algorithm. It is hoped that by using multiple wavelengths simultaneously, rather than separately, as in the original proposed algorithm, we can eliminate the periodicity in the PtV values with respect to the piston error.

For the broadband algorithm, we use light in a Gaussian bandpass. The optical path difference introduced between the arms of the interferometer is now taken to be 1/4 of the central wavelength. The width of the Gaussian band-pass may be modified and will be discussed in the analysis. Again, analysis of changes in the PtV value is used to determine the piston error.

Mathematical Background
Since the setup for the broadband Mach-Zehnder algorithm is virtually identical to the monochromatic algorithm, we may make use of our previous derivations with minimal modification to account for the change in bandpass.

Equation 4 still applies in the broadband case, except that the intensity V is no longer a constant, but is a function of wave number k. Keeping in mind that the optical path difference α is taken to be 1/4 of the central wavenumber k_0, the above equation can be re-expressed to give the PtV of a single wavelength in the broadband case as:

$$v(\delta) = V \cos[k(\delta + \alpha)] \qquad (6)$$

where $V(k)$ corresponds to a Gaussian distribution centered about k_0:

$$V(k) = \exp[\frac{-(k - k_0)^2}{2\sigma^2}] \qquad (7)$$

σ is given by:

$$\sigma = \frac{\pi}{\sqrt{8\ln(2)}} \frac{2\Delta\lambda}{\lambda_0^2} \qquad (8)$$

where $\Delta\lambda$ is the width of the Gaussian distribution (in microns), and λ_0 is the central wavelength of the Gaussian (in microns).

Thus, summing over all the wavelengths, the result is an integral over infinity for the broadband PtVs:

$$v(\delta) = \int V(k) \cos[k(\delta + \alpha)] dk \qquad (9)$$

Evaluating this integral (Gradshtein et al., 1994), we finally obtain our new equation for the broadband Mach-Zehnder algorithm:

$$v(\delta) = \sigma\sqrt{2\pi} \exp[\frac{-\sigma^2(\delta + \alpha)^2}{2}] \cos[k_0(\delta + \alpha)] \quad (10)$$

Given that we have set the optical path difference α to $\lambda_0/4$, it is clear that our values for PtV in the broadband case behave as a sine wave modulated by a Gaussian distribution. Thus, our PtV values are no longer periodic, but decay as the piston error increases.

Simulation
The original simulation for the monochromatic algorithm can be easily modified for the broadband setup, much as the equations were modified in the previous section. Note that there is an integral over infinity when summing the contributions from each wavelength of light.

The complex amplitudes are calculated at the interferograms using the FFT for several equally-spaced values of λ between the central wavelength λ_0 and a distance that is at least as wide as our Gaussian bandpass $\Delta\lambda$, with the optical path difference for each wavelength set to $\lambda_0/4$. Since the contributions from the different wavelengths add incoherently, each complex amplitude is squared separately to find the intensities before summing them, with each intensity scaled by the appropriate value determined by the Gaussian bandpass.

Simulation Results
The PtV values plotted with respect to piston error converge to the values predicted by the mathematical model as

the number of wavelength steps used in the calculation, and the spread of wavelength values for which they are calculated, are increased. A plot of the PtV at physical step heights of $(n/20)\lambda_0$ (where n is an integer) correlates with the predicted model (Figure 5).
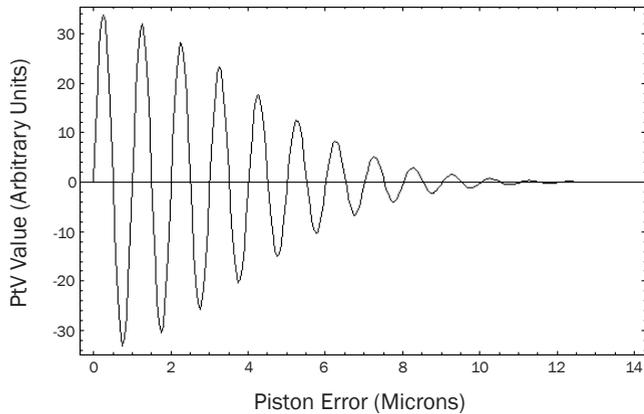

Figure 5
Results of PtV (vertical axis) plotted with respect to the piston error (horizontal axis) for broadband case.

The convergence can be more clearly seen by a comparison of the predicted and simulated values at the maxima of each cycle, i.e. piston errors of $(n + 1/4)\lambda_0$. This gives the "envelope" of the PtV function demonstrating the rate of decay as piston error increases (Figure 6).
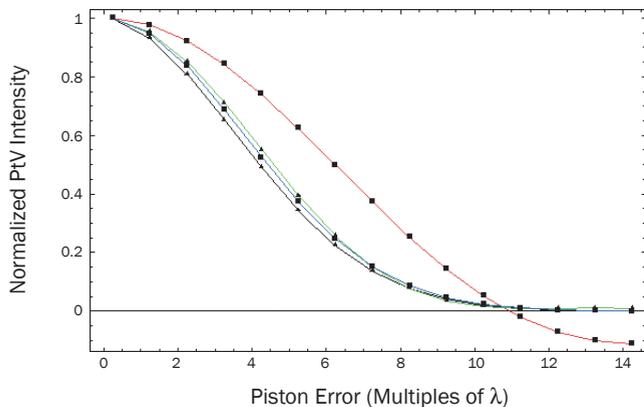

Figure 6
Convergence of simulated (black) and predicted PtV modulating envelope at values of the piston error equal to $(n + 0.25)\lambda$, calculated using different numbers of wavelength steps. The red line indicates results for wavelength values spread over 0.5 times width of Gaussian bandpass, green for wavelength values over 1.0 times Gaussian width, and blue for wavelength values over 2.0 times Gaussian width.

Analysis
The above plots both illustrate that the PtV values are no longer periodic with respect to the piston error but are modulated by the Gaussian distribution given by:

$$\exp[\frac{-\sigma^2(\delta+\alpha)^2}{2}] \qquad (11)$$

This decay in PtV as the piston error increases effectively solves the problems associated with the strictly periodic nature of the monochromatic algorithm. No longer are points separated by λ indistinguishable from one another. With the broadband algorithm it is no longer necessary to take multiple readings at different wavelengths except perhaps as an additional check or to detect exceptionally large piston errors. Nevertheless, it is necessary to piston each segment by a known amount and make repeated measurements in order to determine one's position on the modulating function.

As an additional confirmation of the results, the response of the PtV values as the width of the Gaussian bandpass is varied was also observed. As the width of the Gaussian bandpass decreases, the width of the Gaussian "envelope" increases. In the case that the Gaussian bandpass becomes a delta function (width approaches 0), the broadband results reduce to the monochromatic results discussed in the previous section, that is to say the PtV values simply behave as a sine function.

Using the broadband setup, a typical phasing algorithm might consist of pistoning a mirror segment through a distance of one wavelength in an attempt to locate a local maximum [located every $(n + 0.25)\lambda$]. Once a maximum has been detected, the segment may then be pistoned in steps equal to one wavelength, thus allowing determination of location on the Gaussian modulating the PtV values as discussed above.

Future Work

Work still remains to be done before this algorithm can be successfully applied in the field. The full effects of the size of the pinhole in the interferometer have not yet been thoroughly tested. In general, the width of the fringes in the differential interferogram from which the PtV values are calculated is inversely related to the width of the pinhole, as expected from the uncertainty principle. For the purposes of the simulation above, the width of the Gaussian profile of the pinhole was taken to be 100 pixels in diameter, the

total image being a 512 by 512 pixel array. This provided fringes that were judged to be of an ideal width.

Some factors were ignored in the simulation for the purposes of simplicity. The study ignored tip/tilt errors and assumed that all errors are in the piston; the effects of atmospheric blurring warrant further study. Martinez *et al.* cover the effects of some of these factors on the monochromatic algorithm in their original paper (2002).

Conclusions

The monochromatic Mach-Zehnder phasing algorithm proposed by Martinez *et al.* (2002) has been implemented via computer simulation. The piston error between adjacent segments of a segmented telescope mirror has been shown to be related to the resulting PtV value. Through the simulation results and the mathematical equations involved, a significant ambiguity in measurement of piston error has been shown to exist when this algorithm is used, especially when the piston errors are large.

A broadband modification to the Mach-Zehnder algorithm involving the use of a Gaussian bandpass has also been proposed and detailed. It has been shown that in the broadband case, the PtV values decay to zero as the piston error increases, thus removing the ambiguity in the monochromatic case and allowing the measurement of large piston errors. The broadband Mach-Zehnder algorithm is ideal because it combines the benefits of both the monochromatic algorithm and the Keck algorithm while avoiding problems associated with both.

The needs of astronomers have often been one of the greatest driving forces behind the development of optical technology, from Galileo's first crude telescopes to the development of the extremely large telescopes and adaptive optics of the late twentieth and early twenty-first centuries. As with the case of nearly all fields of science, technological innovations originally intended for astronomy have often found uses outside their original field in other branches of science, medicine and engineering. Ultimately, this phasing algorithm makes it an interesting alternative to existing algorithms for use in segmented mirrors both on Earth and in space.

Acknowledgements

Works Cited

Chanan, G. "Phasing the Mirror Segments of the Keck Telescopes: the Broadband Phasing Algorithm," Applied Optics 37 (1988): 140-155.

Chanan, G. Phasing the Keck Telescope. Retrieved May 25, 2004, from http://www.ps.uci.edu/physics/news/chanan.html .

Gradshtein, I.S., I.M. Ryzhik, and A. Jeffery. Table of Integrals, Series, and Products. Boston, 1994. 514.

Hecht, E. Optics. 4th Edition Reading, Massachusetts, 2001.

Martinez, L.M., N. Yaitskova, P. Dierickx, and K. Dohlen. (2002, October 11). Mach-Zehnder Wavefront Sensor for Phasing of Segmented Telescopes. Retrieved May 25, 2004, from http://www.eso.org/projects/owl/publications/2002_Hawaii_Mach_Zehnder.pdf .

Nelson, J. "The Keck Telescope," American Scientist, 77 (1989): 170-176.

Nelson J., T. Mast, and S. Faber, eds. "The Design of the Keck Observatory and Telescope." Keck Observatory Report 90 (1985): 1-6.